



## RESEARCH ARTICLE

10.1029/2019WR026750

# Diversion of Flow and Sediment Toward a Side Channel Separated From a River by a Longitudinal Training Dam

T. V. de Ruijsscher<sup>1</sup> , B. Vermeulen<sup>1</sup> , and A. J. F. Hoitink<sup>1</sup> <sup>1</sup>Hydrology and Quantitative Water Management Group, Department of Environmental Sciences, Wageningen University, Wageningen, The Netherlands

## Key Points:

- Depth variation of the flow at the intake of a side channel with a constructed sill is steered by the geometry of the sill
- Horizontal flow pattern in the side channel entrance region is qualitatively similar to free flow over a sharp-crested side weir
- A constructed sill is of vital importance for the morphological stability of the side channel behind a longitudinal training dam

## Correspondence to:

A. J. F. Hoitink,  
ton.hoitink@wur.nl

## Citation:

de Ruijsscher, T. V., Vermeulen, B., & Hoitink, A. J. F. (2020). Diversion of flow and sediment toward a side channel separated from a river by a longitudinal training dam. *Water Resources Research*, 56, e2019WR026750. <https://doi.org/10.1029/2019WR026750>

Received 12 NOV 2019

Accepted 1 MAY 2020

Accepted article online 7 MAY 2020

**Abstract** A human-made entrance to a side channel separated from the river by a longitudinal training dam can be considered a new, emergent type of river bifurcation. To understand the processes controlling the diversion of flow and sediment toward the side channel at such bifurcations, a comprehensive field monitoring program was performed in the Waal River, which is the main branch of the Rhine River in the Netherlands. Local processes govern the flow field in the bifurcation region. The angle between the main river flow and the flow into the side channel increases with decreasing lateral and longitudinal distance to the bifurcation point, which corresponds to the head of the training dam. The general flow pattern can be well reproduced with a uniform depth, potential flow model consisting of a superposition of main channel flow and lateral outflow. For submerged flow conditions over the sill, the side channel hydraulic conditions influence the exchange processes, yet free flow side weir theory describes the flow field at this bifurcation type qualitatively well. The vertical flow structure in the side channel, which governs the sediment exchange between the main channel and the side channel, is steered by the geometrical details of the sill. The presence of the sill structure is key to controlling the morphological stability of this type of bifurcation given its primary influence on bed load sediment import and exerts an indirect impact on suspended sediment exchange.

## 1. Introduction

Bifurcations in natural and man-made systems control the division of water and sediment over the downstream branches. In nature, bifurcations occur in alluvial fans, braided rivers, fluvial lowland plains, and deltas (Kleinhans et al., 2013), whereas flow division in man-made systems occurs in side-channel spillways (Bremen & Hager, 1989), in lateral outflow channels (Neary & Odgaard, 1993), and at the entrance of side channels (van Denderen et al., 2018). All these bifurcation systems have been extensively studied to address their morphological evolution, which depends on the water and sediment distribution over the two downstream branches. Here, we study a new, emergent type of river bifurcation with a side weir: the entrance of a side channel separated from the river by a longitudinal training dam (LTD) with a bifurcation angle close to zero and a rip-rap sill at the upstream end of the side channel (Figure 1).

A bifurcation is classified as morphologically stable if both downstream channels remain open over the time scale of a century. For typical bed shear stresses in sand bed rivers, symmetrical bifurcations are typically unstable, and one of the channels will eventually dominate (Bolla Pittaluga et al., 2015) as a result of the Bulle effect: The curved flow forces a disproportionately large amount of sediment into one of the channels, which is a self-enforcing effect (Bulle, 1926; Blanckaert et al., 2013; Dietrich & Smith, 1984; Dutta, 2017).

Various stabilizing mechanisms have been proposed for asymmetric bifurcations, of which we expect following mechanisms to possibly be of significant importance at the entrance of an LTD side channel with upstream side weir. A transverse bed slope directs bed load sediment transport toward the lower channel (Bolla Pittaluga et al., 2003; Edmonds & Slingerland, 2008) or prevents sediment from being transported over a sill. Such a sill acts as an inlet step, which can prevent sediment in the lower part of the water column from entering an off-take channel (Kästner & Hoitink, 2019; Slingerland & Smith, 1998). Abandoning of one of the downstream channels is influenced by the bifurcation angle (Mosselman et al., 1995; van Denderen et al., 2018), where a small-angle bifurcation is more likely to be stable (Hardy et al., 2011). For side channels where the bifurcating, smaller channel reattaches to the main channel at a downstream location,

©2020. The Authors.

This is an open access article under the terms of the Creative Commons Attribution License, which permits use, distribution and reproduction in any medium, provided the original work is properly cited.

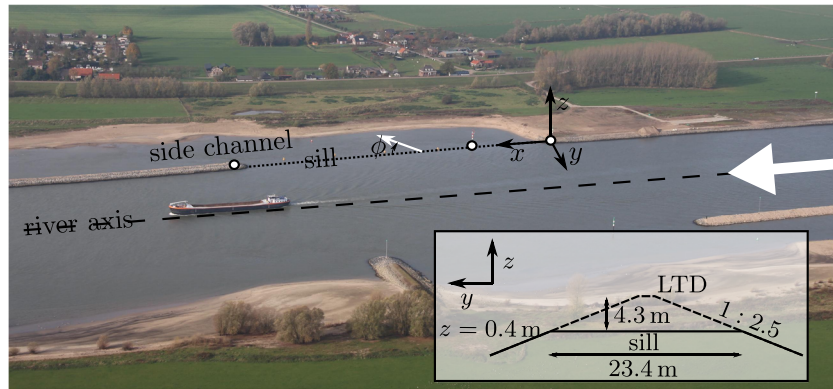


**Figure 1.** Field campaign location, with main channel flow from right to left. White dots indicate three poles, which will be used as spatial references throughout this paper. The sill is located upstream of and in line with the LTD. The inflow angle into the side channel is denoted by  $\phi$ . Inset: cross section of sill and LTD in the  $(y, z)$  plane. Photo courtesy: Rijkswaterstaat Oost-Nederland.

the side channel becomes increasingly dominant for decreasing relative side channel length (van Denderen et al., 2018). The stability of parallel side channels as created by LTDs appears to depend on the location of the bifurcation with respect to the top of nonmigrating bars (Le, Crosato, & Uijtewaal, 2018; Le, Crosato, Mosselman, et al., 2018).

Flow patterns at high-angle bifurcations with bifurcation angles close to  $90^\circ$  depend on the Froude number and the water level ratio between the main channel (upstream) and the lateral outflow channel (Neary & Odgaard, 1993; Ramamurthy & Satish, 1988). A horizontal flow separation cell with accompanying sedimentation was observed both numerically (Neary & Odgaard, 1993; Neary et al., 1999) and experimentally (Barkdoll, 1997). Often, a side weir is present at the entrance of such a lateral outflow channel. Side weirs have been extensively studied regarding their effect on the water level profile and discharge regulation (El-Khashab & Smith, 1976; Hager & Volkart, 1986; Hager, 1987; Michelazzo et al., 2016; Paris et al., 2012), and their discharge distribution is well described by empirical formulas (Bos, 1976; Lee & Holley, 2002; Paris et al., 2012). However, the obtained results are strictly valid for the experimental conditions under study, which are mostly free flow conditions for short, high, sharp-crested weirs.

The detailed flow pattern in proximity to a side weir is not well understood, but the angle between the main river flow and the flow direction over the weir is thought to increase with (1) decreasing transverse distance to the weir, (2) decreasing vertical distance to the weir, and (3) decreasing lateral distance to the bifurcation point (Figure 2) based on free flow experiments (Hager & Volkart, 1986; Hager, 1987). Hager (1987) is the only study taking into account variations in the Froude number along the weir. However, for quantitative application under submerged conditions, a submergence correction factor is needed for correction of the discharge distribution for plain weirs (Villemonte, 1947), oblique weirs (Borghesi et al., 2003), and side weirs (Lee & Holley, 2002).

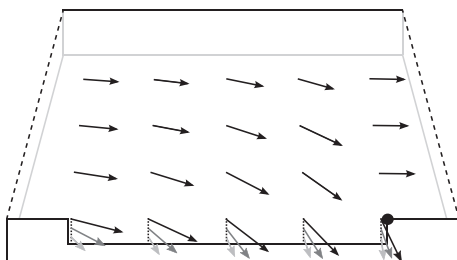


**Figure 2.** Schematic representation of the flow in a channel with a thin-plate side weir under free flow conditions based on Hager (1987). Lighter arrows are located deeper in the water column and the black dot represents the bifurcation point.

The bifurcation studied here is characterized by a side channel separated from the river by an LTD with a sill at the upstream end of the side channel. LTDs have been used as an alternative method of river training in the Loire River (France), the Elbe River (Germany), and the Rhine River (Germany). In the Netherlands, they have recently been introduced to improve multiple river functions through one integral measure: increasing the fairway depth during low water levels (shipping), decreasing the flood risk during high water levels (flood safety), and improving the ecological value of the river system (ecology) (Collas et al., 2018; Eerden et al., 2011; Havinga, 2016; Huthoff et al., 2011).

Water and sediment division over the two channels can be steered by adapting the geometry of the sill at the bifurcation (de Ruijsscher et al., 2019); however, little is known about the spatial flow pattern at very low-angle bifurcations with a sill at the side channel entrance. We do

**Table 1**

*Overview of the Measurement Campaigns Performed in the Study Area, Including s(panwise) or  $\ell$  (ongitudinal) Orientation, Water Level  $z_w$  at the City of Tiel (5 km Upstream), Submergence of the LTD Crest, Number of Profiles  $N$ , m(ain) and/or s(ide) Channel, and ADCP Frequency  $f$*

Date	Orientation	$z_w$ (m)	LTD subm.	$N$	Channel	$f$ (kHz)
11/10/2018	s	2.2	×	9	m	600
				14	s	1200
20/07/2018	$\ell$	2.7	×	3	m	600
12/09/2017	$\ell$	3.9	×	7	m + s	600
07/03/2018	$\ell$	4.2	×	7	m + s	600
16/02/2018	$\ell$	5.1	×	7	m + s	600
05/12/2017	$\ell$	5.4	×	7	m + s	600
01/12/2017	$\ell$	6.1	✓	6	m + s	600
02/02/2018	$\ell$	7.4	✓	7	m + s	600

*Note.* Dates are formatted as DD/MM/YYYY.

hypothesize, however, that the flow pattern for the low-angle bifurcation with a dike-shaped, broad-crested side weir as present at LTDs qualitatively resembles the free flow over a sharp-crested side weir (Figure 2) even without applying a submergence correction factor. This presumption is strengthened by the observation of a flow separation cell downstream of the side weir by both de Ruijsscher et al. (2019) (submerged side weir) and Hager (1987) (free-flow side weir). Even less is known about suspended and bed load sediment transport associated with the flow over submerged side weirs, although it is of crucial importance for side channel stability. We expect the sediment transport, in analogy with the flow, to depend on the geometrical properties of the weir (length, side slope, and height) and the morphological stability to be reasonably well described by side channel and bifurcation stability theory (Kästner & Hoitink, 2019; van Denderen et al., 2018).

In this paper, we aim to understand the processes controlling the diversion of flow and sediment toward a side channel separated from the river by a LTD. For this purpose, we provide a conceptual model for flow patterns in the bifurcation area (main and side channel) based on field measurements, and we compare the flow patterns with results of an analytical potential flow model. We link the obtained results to existing knowledge on side weirs and bifurcations at side channel entrances to determine what mechanisms are dominant for flow and sediment transport in the present case study. This can ultimately lead to better predictions of flow and sediment diversion into LTD-type side channels. After introducing the study area and methods in section 2, a data analysis of flow and sediment transport is presented in section 3, along with flow predictions from a potential flow model. Section 4 provides a discussion with feedback to the hypotheses, coupled to results from the literature, where the relevant processes are situated in a conceptual model. Finally, conclusions are given in section 5.

## 2. Methods

### 2.1. Study Area

In the present study, we focus on LTDs in the Waal River (the Netherlands), the main branch of the Rhine in the Netherlands. LTDs align with the main flow direction in the fairway, thus separating the main channel from a bank-connected side channel with a sill at the bifurcation of the main and side channels (Figure 1). This sill aligns with the river axis and might therefore be considered as a broad-crested side weir. However, for clarity, we will use the term “sill” for the case of LTDs, whereas the term “weir” will be used in a more general context. During high discharges (approximately 100 days a year), the water level exceeds the crest height of the LTD.

We focus on the most downstream of three LTDs and the only one on the right side of the river. The side channel has a width of 90 m on average and the sill length is 243 m. Poles are located for navigational purposes at both the upstream and downstream ends of the sill. A third pole with measurement equipment attached is located at a distance of 66 m from the upstream end of the sill. These three poles will be consistently indicated as black dots in the graphs throughout this paper for geographical reference. Earth coordinates

**Table 2**

Overview of Flow Characteristics for the Measurement Campaigns Listed in Table 1: Total Discharge  $Q_{tot}$ , Side Channel Discharge as a Fraction of the Total Discharge  $\frac{Q_{side}}{Q_{tot}}$ , Typical Water Depth  $d$  and Froude Number  $Fr$

date	$Q_{tot}$ ( $m^3 s^{-1}$ )	$\frac{Q_{side}}{Q_{tot}}$	$d$ (m)			$Fr$		
			Upstream	Main	Side	Upstream	Main	Side
11/10/2018	683	0.18	3.5	3.4	2.4	0.15	0.15	0.10
20/07/2018	976	0.19	4.2	4.2	3.2	0.16	0.14	0.11
12/09/2017	1381	0.20	5.1	5.0	3.3	0.16	0.15	0.15
07/03/2018	1420	0.21	5.2	5.2	4.8	0.16	0.14	0.09
16/02/2018	1937	0.25	6.0	6.0	5.0	0.16	0.14	0.13
05/12/2017	2070	0.25	6.1	6.7	5.3	0.15	0.13	0.14
01/12/2017	2183		(from $(Q, h)$ -relation at Tiel, 5 km upstream)					
02/02/2018	3388	0.27	7.7	6.5	6.0	0.15	0.14	0.14

*Note.* The latter two are provided for upstream, main channel, and side channel conditions. Dates are formatted as DD/MM/YYYY.

$(x_{RD}, y_{RD})$  in the EPSG 28992 system have been rotated and translated to a Cartesian  $(x, y)$  system with the origin at the upstream end of the sill and the  $x$  axis aligned with the sill (Figure 1).

## 2.2. Field Data

Flow velocities have been measured using an acoustic Doppler current profiler (ADCP) attached to a vessel. Emitted and reflected sound pulses from the ADCP are translated into water flow velocities, making use of the Doppler effect. An overview of the measurement campaigns is shown in Table 1, with accompanying flow characteristics in Table 2. Water samples are only taken during the measurement campaign of 11 October 2018 in the main channel and converted to the whole 3-D ADCP measurement reach via linear regression with the ADCP backscatter strength (Hill et al., 2003; Hoitink & Hoekstra, 2005; Holdaway et al., 1999). For this, the volume backscatter strength  $S_v$  (in dB) is calculated using the sonar equation (Deines, 1999), following, for example, Hoitink and Hoekstra (2005) and Sassi et al. (2012),

$$S_v = 2\hat{\alpha}R + K_c (E - E_r) + C_S \log_{10} \left( \frac{T_T R^2}{L P_T} C_T \right) + C, \quad (1)$$

in which  $R$  denotes the range along the beam axis to the scatterers (in m),  $\hat{\alpha} = 0.3323 \text{ dB m}^{-1}$  is the attenuation coefficient,  $E$  is the echo strength (in counts),  $E_r = 40$  counts is received noise,  $K_c = 0.45 \text{ dB count}^{-1}$  is a scale factor,  $T_T$  is the transducer temperature (in K),  $L$  is the transmit pulse length (in m),  $P_T$  is the transmit power (in W),  $C$  is a constant (in dB),  $C_S = 10 \text{ dB}$ , and  $C_T = 1 \text{ kg m K}^{-1} \text{ s}^{-3}$  to make the argument of the logarithm nondimensional. Afterward, the suspended sediment concentration (in  $\text{mg L}^{-1}$ ) is calculated from

$$\frac{SSC}{\text{mg L}^{-1}} = 10^{aS_v + b}, \quad (2)$$

with  $a = 0.043 \text{ dB}^{-1}$  and  $b = 2.891$ . The value of  $a$  is fixed based on field experience of the measurement company and closely matches the value found by Hoitink and Hoekstra (2005). The value of  $b$  is obtained by linear regression of the data in  $(S_v, \log_{10} SSC)$  space.

Bed samples have been gathered using a Hamon grab (Eleftheriou & Moore, 2013; Oele, 1978) on 24 and 27 November 2017 in the main and side channels, respectively. Figure 3 provides an overview of the location of longitudinal profiles (example shown: 16 February 2018) and lateral profiles (11 October 2018) along with the locations where bed samples were taken on 11 October 2018.

## 2.3. Analysis Methods

Raw ADCP data were processed using the improved method of Vermeulen et al. (2014), implemented in the Matlab ADCPtools toolbox, allowing for better retrieval of near-bed velocities. We corrected for ship velocity by using a bottom-tracking algorithm. Using this method, we assumed that the bed did not significantly change during each of the measurement campaigns, which appeared to be a valid assumption.

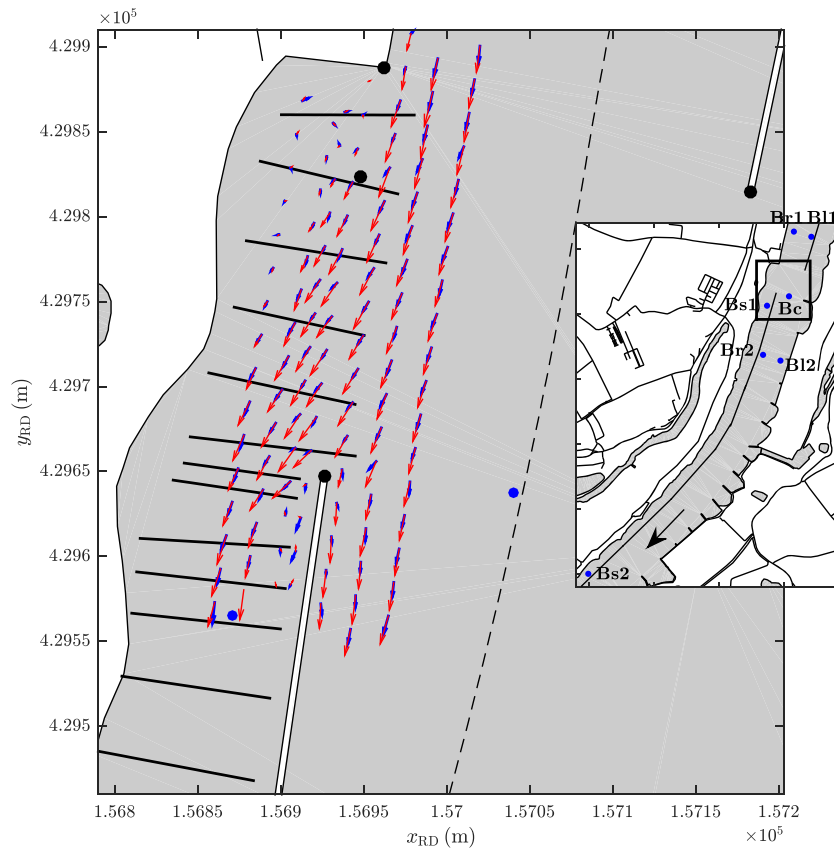


**Figure 3.** Flow vectors in the lower (blue) and upper (red) half of the water column. Measurements taken on 16 February 2018 at a water level at Lobith of  $z_w = 9.8$  m. The dashed line indicates the river axis, and solid lines indicate the measured cross sections at 11 October 2018. Inset: location of bed samples of November 2017 (blue dots).

For the largest part of the water column, a logarithmic velocity profile holds as a good approximation:

$$u = \frac{u_*}{\kappa} \ln \left( \frac{z}{z_0} \right), \quad (3)$$

in which  $\kappa = 0.4$  is the Von Kármán constant (von Kármán, 1930),  $z$  is the distance from the bed, and  $z_0$  is a characteristic roughness height. In river hydraulics, the characteristic velocity  $u_*$  is set to be equivalent to the bed shear velocity, although this strictly only holds for uniform 2-D flow (Smart, 1999). Under this assumption, the bed shear velocity  $u_*$  can be determined from the slope of the vertical velocity profile in  $(\log_{10} z, |\bar{u}|)$  space.

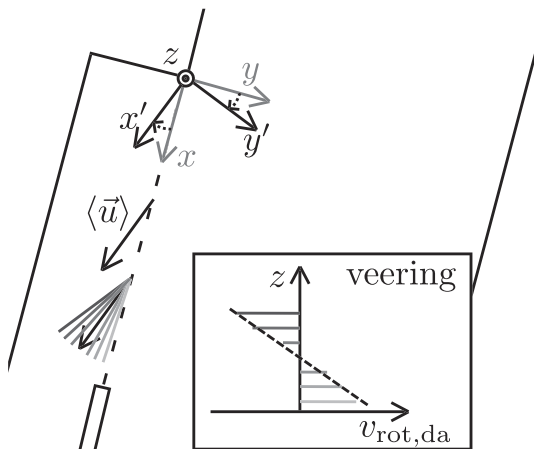


**Figure 4.** Coordinate transformation by rotation of  $x$  toward the depth-averaged flow direction (top) and definition of veering of the flow as  $\langle \partial v_{rot,da} / \partial z \rangle < 0$ , where  $v_{rot,da}$  is the velocity component along the  $y'$  axis.

To examine the horizontal rotation of the flow, a coordinate transformation is first applied by rotation around the  $z$  axis toward the direction of the depth-averaged flow  $\langle \bar{u} \rangle$  ( $x'$  axis, Figure 4). This results in a rotated velocity vector  $\bar{u}_{rot,da} = (u_{rot,da}, v_{rot,da}, w)$ . The first two components of  $\bar{u}_{rot,da}$  represent the horizontal velocity in  $(x', y')$  space: along and orthogonal to  $\langle \bar{u} \rangle$ , respectively. The variation in  $v_{rot,da}$  over depth defines veering or backing of the flow velocity vector as

$$\begin{aligned} \omega_{x'} &= \frac{\partial v_{rot,da}}{\partial z} < 0 && \text{veering (Figure 4)}, \\ \omega_{x'} &= \frac{\partial v_{rot,da}}{\partial z} > 0 && \text{backing}, \end{aligned} \quad (4)$$

assuming  $\partial w / \partial y'$  is negligible. In the present study, we applied a linear fit in  $(v_{rot,da}, z)$  space to obtain a depth-averaged value  $\langle \omega_{x'} \rangle$ .

The bed sample data were fitted to a sigmoid curve in  $(\log_{10}D, p_s)$  space:

$$p_s = \left( 1 + \exp \left[ -\frac{S_p}{4} \log_{10} \left( \frac{D}{D_{50}} \right) \right] \right)^{-1}, \quad (5)$$

in which  $p_s$  is the sieve throughfall fraction,  $D$  is the sediment diameter,  $D_{50}$  is the median sediment diameter, and  $S_p$  is the slope of the sigmoid curve at  $D = D_{50}$ .  $S_p$  and  $D_{50}$  were used as fitting parameters, and the 90th percentile sediment diameter  $D_{90}$  was derived as

$$D_{90} = 10^{4 \ln 9 / S_p} D_{50}. \quad (6)$$

A generally used criterion to judge whether sediment could go into suspension is the quotient of the shear velocity and settling velocity,  $u_* / w_s$ . The latter is defined as the terminal velocity of a falling particle. Various critical values for  $u_* / w_s$  are reported in the literature, including  $u_* / w_s = 0.8$  (Bagnold, 1966) and  $u_* / w_s = 0.4$  (van Rijn, 1984). Despite this range of critical values, evaluation of  $u_* / w_s$  still provides a good indication for the onset of suspended sediment transport. The shear velocity is obtained from a first-order polynomial bisquare robust fit using equation (3). The settling velocity is determined using the method of Cheng (2009):

$$\begin{aligned} w_s &= \sqrt{\frac{4}{3} \frac{\rho_s - \rho_w}{\rho_w} \frac{g D_{50}}{C_d}}, \\ C_d &= \frac{432}{D_*^3} (1 + 0.022 D_*^3)^{0.54} + 0.47 (1 - \exp[-0.15 D_*^{0.45}]), \\ D_* &= D_{50} \left( \frac{\rho_s - \rho_w}{\rho_w} \frac{g}{\nu^2} \right)^{1/3}, \end{aligned} \quad (7)$$

in which  $\rho_s$  is the sediment density,  $\rho_w$  is the water density,  $g$  is the gravitational acceleration, and  $\nu$  is the kinematic viscosity.

#### 2.4. Potential Flow Model

The analytical potential flow model for side channel outflow as discussed by Kästner (2019) is used in the present study. They assumed a rectangular cross section of the main channel with uniform depth and represented the diversion as a rectangular section with the same width as the main channel. Neglecting friction and secondary flow, and assuming a small Froude number and an infinitely long main channel ( $L \rightarrow \infty$ ), the following boundary conditions hold

$$\begin{aligned} u(-\infty, y) &= u_0 + \frac{1}{2} \frac{w_s}{w_0} \frac{v_0}{u_0}, \\ u(\infty, y) &= u_0 - \frac{1}{2} \frac{w_s}{w_0} \frac{v_0}{u_0}, \\ v(x, w_0) &= 0, \\ v(x, 0) &= v_0 f, \end{aligned} \quad (8)$$

where  $w_0$  is the width of the main channel,  $w_s$  is the width of the side channel inlet,  $f$  is the velocity profile across the inlet fulfilling  $\int_{-\infty}^{\infty} f dx = w_s$ , and  $v_0$  is the velocity averaged across the inlet. The governing equation under these assumptions appears to be the Laplace equation:

$$\nabla^2 \Phi = 0, \quad (9)$$

with the flow potential  $\Phi$  determining the flow velocity as  $u = \partial \Phi / \partial x$  and  $v = \partial \Phi / \partial y$ . Finally, an algebraic solution is obtained for the limiting case of an infinitely wide channel ( $w_0 \rightarrow \infty$ ) and a constant profile  $f = 1$ . In terms of the normalized coordinates  $\hat{x} = x / w_s$  and  $\hat{y} = y / w_s$  this solution reads

$$\begin{aligned} u &= u_0 \left[ 1 - \frac{\alpha}{2\pi} \ln \left( \frac{\hat{x}^2 + \hat{y}^2}{(\hat{x} - 1)^2 + \hat{y}^2} \right) \right], \\ v &= u_0 \left[ -\frac{\alpha}{\pi} \arctan 2(-\hat{y}, \hat{x}^2 + \hat{y}^2 - \hat{x}) \right], \end{aligned} \quad (10)$$

where  $\alpha = v_0 / u_0$  and  $\arctan 2$  is the unambiguous two-argument arctangent function.

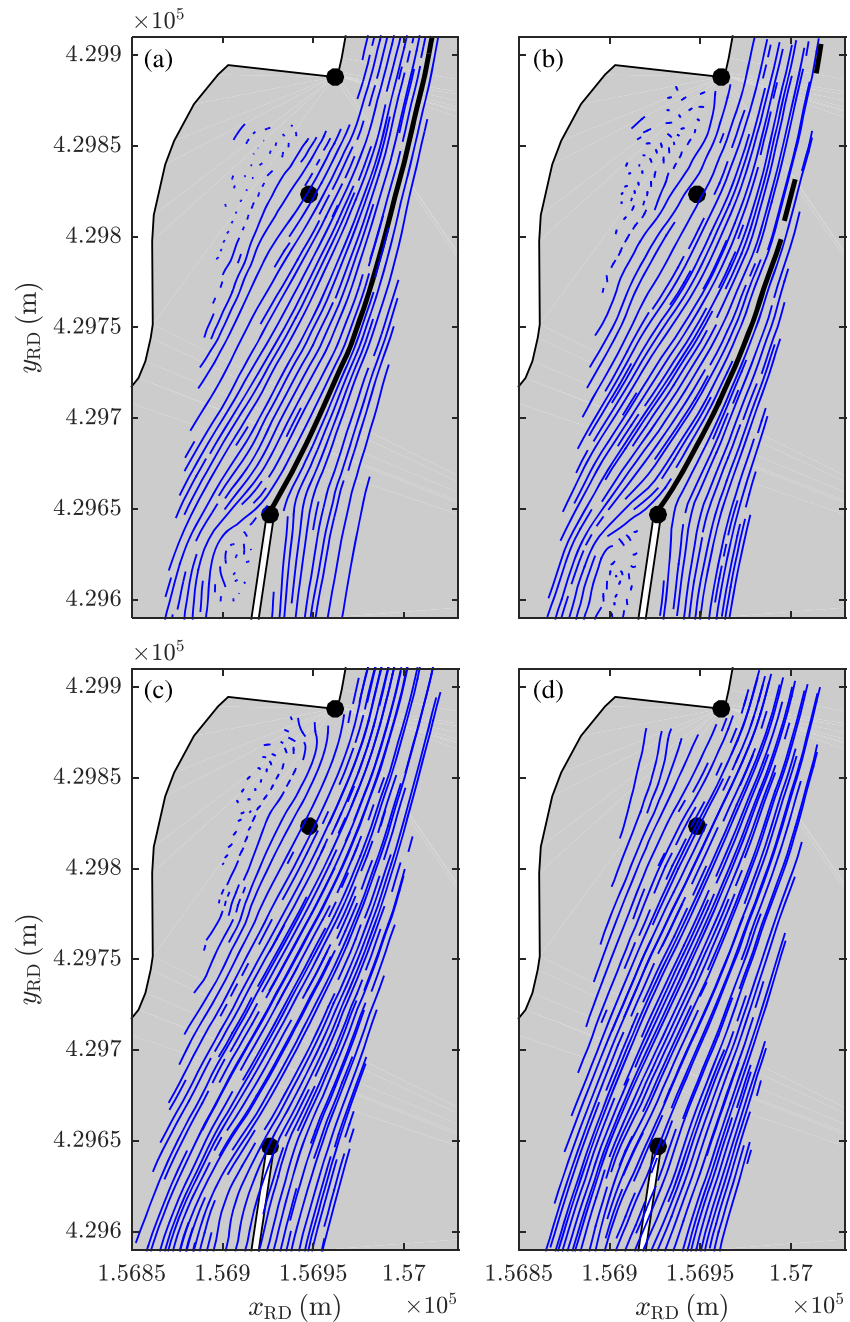


**Figure 5.** Streamlines (blue curves) over the sill at the side channel entrance with flow velocities averaged over the top half of the water column. The thick black curves indicate the dividing streamlines, and black dots indicate navigation poles. Four different water levels at Tiel (5 km upstream): (a)  $z_w = 4.2$  m (7 March 2018), (b)  $z_w = 5.1$  m (16 February 2018), (c)  $z_w = 6.1$  m (1 December 2017), and (d)  $z_w = 7.4$  m (2 February 2018).

### 3. Results

#### 3.1. Flow of Water Over a Side Weir

##### 3.1.1. Horizontal Flow Variation

The flow near the LTD is streamlined and two distinct features are observed (Figure 5): an upstream horizontal secondary circulation cell (Figures 5a–5c) and a downstream flow separation zone (Figures 5a and 5b), when the water level is below the LTD crest height. The upstream horizontal secondary circulation cell decreases with increasing water level until it disappears (Figure 5d). The flow separation zone disappears

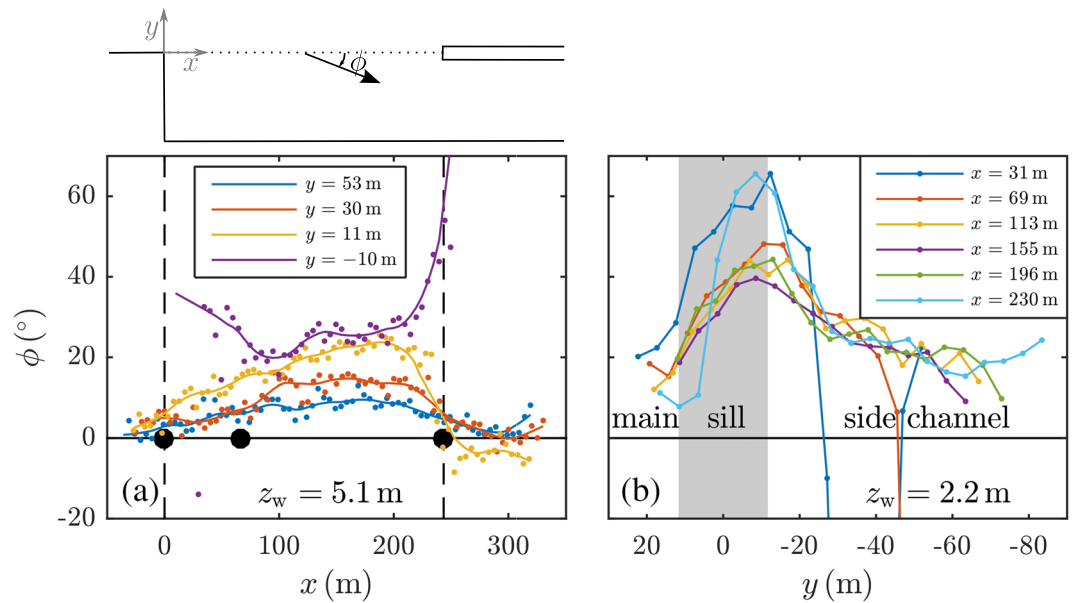


**Figure 6.** Flow angle  $\phi$  over the sill in the upper half of the water column versus (a) longitudinal distance from the upstream end of the sill  $x$  and (b) transverse distance from the sill  $y$ .

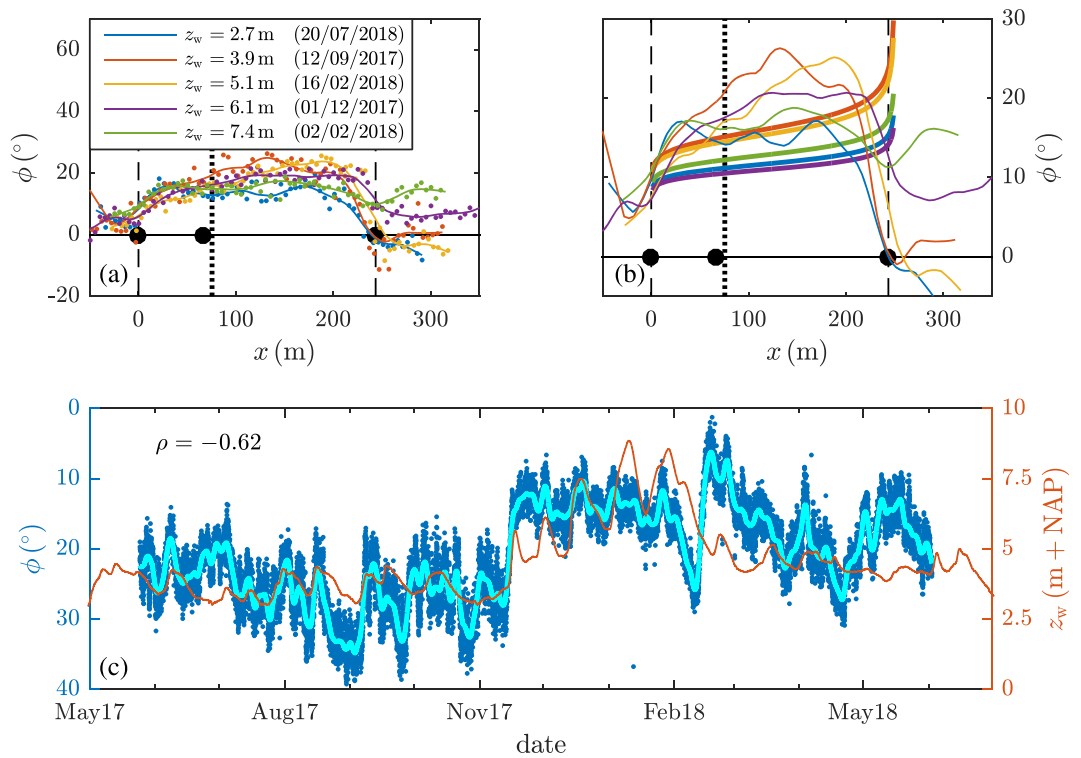


**Figure 7.** (a) Longitudinal variation in flow angle  $\phi$  in the upper half of the water column for the main channel longitudinal profile closest to the sill. Various stages of the hydrograph are shown. Dashed lines denote upstream and downstream ends of the sill. (b) Same as (a) but including the estimate of  $\phi$  over the sill from a potential flow model (Kästner, 2019). (c) Flow angle  $\phi$  (blue) and water level  $z_w$  (red) versus time at 1 m above the LTD sill from H-ADCP data at  $x = 75.5$  m (dotted line in a and b). The thick magenta curve indicates LOESS-averaged  $\phi$  with a filter span of four days, for which correlation  $\rho$  with  $z_w$  is shown.

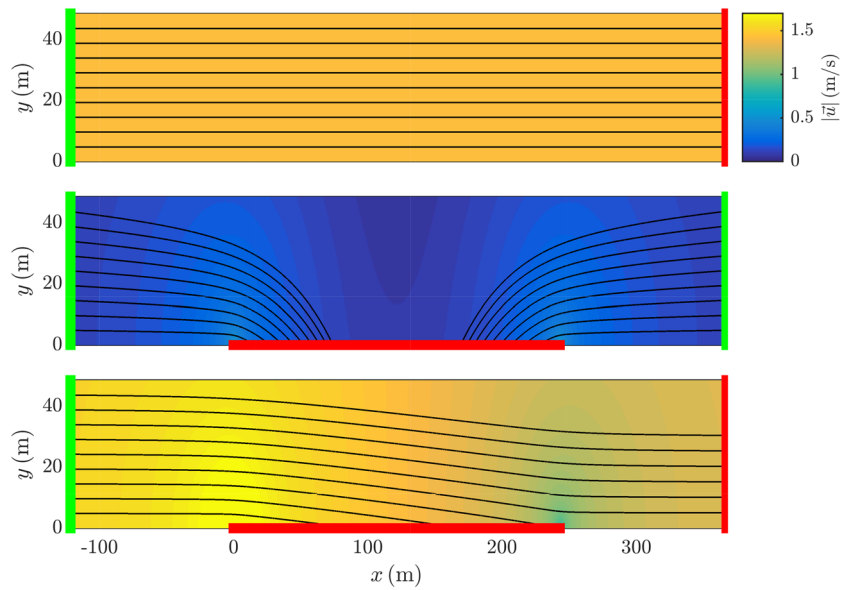


**Figure 8.** Flow magnitude (colors) and streamlines for potential flow (equation (10)) with the dimensions of the present case study, from top to bottom: main channel flow without lateral outflow, lateral outflow component, and total flow pattern, being the superposition of both. Green and red indicate inflow and outflow boundaries, respectively.

when the water level exceeds the LTD crest height, effectively turning the LTD crest into a second submerged weir, similar to the sill.

When the water level is below the LTD crest, the dividing streamline is well defined, which is the streamline that separates the water ultimately flowing into the side channel from the water that remains in the main channel (thick black curves in Figure 5). The location of the dividing streamline does not significantly change for varying water level.

The angle  $\phi$  at which water flows into the side channel (cf. Figure 1) increases in the downstream direction, especially in the main channel ( $y > 0$ ) and outside the upstream horizontal secondary circulation cell in the side channel (Figure 6a). Close to the LTD head ( $x \rightarrow 244$  m or  $\hat{x} \rightarrow 1$ ),  $\phi$  is reduced to 0 or negative values in the main channel, whereas values up to  $60^\circ$  are reached in the side channel.

Spanwise,  $\phi$  reaches its maximum at 5 to 10 m into the side channel, which is still on the plateau of the sill. Maximum values of up to  $\phi = 70^\circ$  are reached at the most upstream and downstream ends of the sill, whereas maximum values of  $40^\circ$  to  $50^\circ$  are reached over the center part of the sill (Figure 6b). The large negative values in the most upstream part of the side channel ( $x = 31$  m and  $x = 69$  m) are due to the presence of a horizontal secondary circulation cell.

Figure 7a shows the inflow angle  $\phi$  for the main channel longitudinal profile closest to the LTD for different water levels. Minimal differences are visible over the length of the sill ( $0 \text{ m} < x < 244 \text{ m}$  or  $0 < \hat{x} < 1$ ) because the variability of  $\phi$  due to water level changes is masked by the overall scatter. When water overtops the LTD crest, at  $z_w = 6.1$  m and  $z_w = 7.4$  m,  $\phi$  increases downstream of the LTD head ( $x > 244$  m or  $\hat{x} > 1$ ) because the streamlines are less blocked by the LTD (see also Figure 5). From H-ADCP measurements over the central part of the sill, it follows that  $\phi$  negatively correlates with the water level, so  $\phi$  decreases with increasing water level (Figure 7c).

### 3.1.2. Predictions From a Potential Flow Model

Both the stationary behavior of the dividing streamline and the form of the pattern resemble an analytical potential flow pattern for side channel outflow as described by equation (10) (Kästner, 2019). When applying the analytical model with the spatial dimensions of the current case study, the resulting flow pattern is qualitatively similar to what is observed in the field (Figure 8). However, the dividing streamline is at a lateral distance of less than 20 m from the sill, whereas this value is close to 50 m in the field (Figures 5a and 5b). This finding is most probably caused by the presence of the sill, which limits the flow cross-sectional area

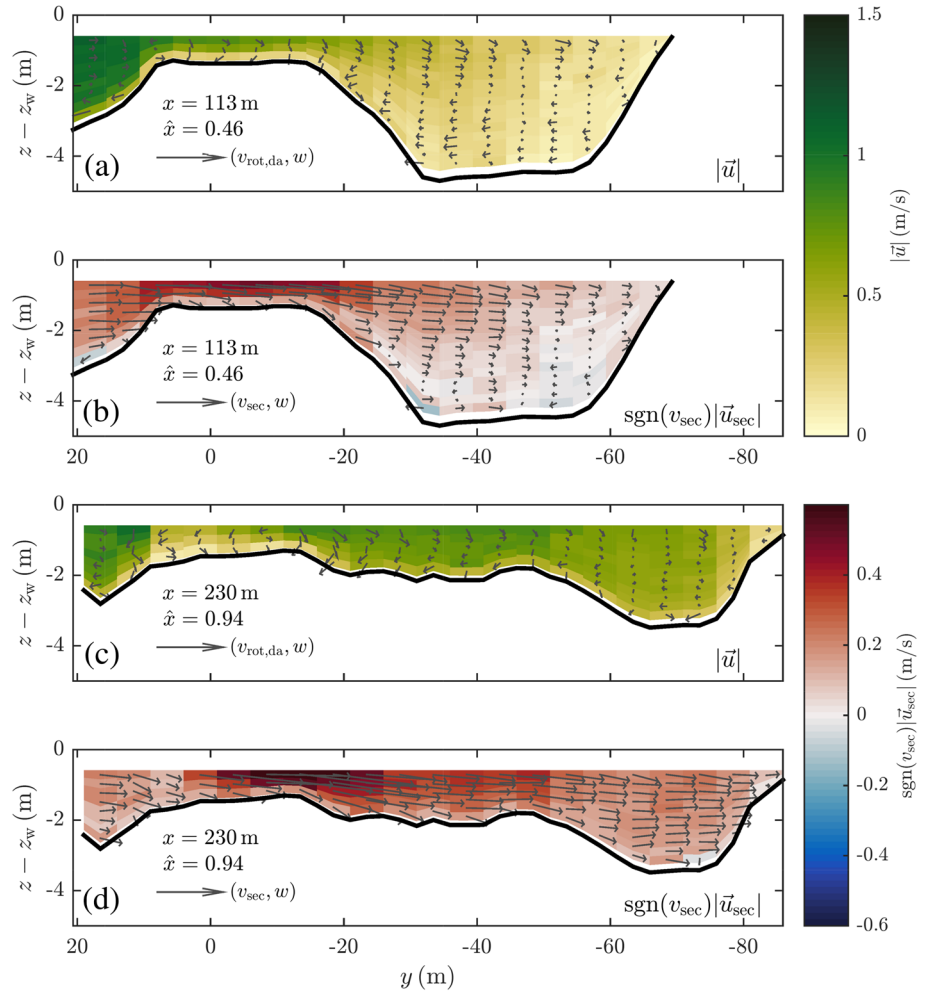


**Figure 9.** Two cross-sectional velocity profiles. (a and c) Absolute velocity magnitude with velocity vectors ( $v_{\text{rot,da}}, w$ ) rotated toward the depth-averaged flow direction (see Figure 4). (b and d) Signed velocity component in the cross-sectional plane, red (blue) indicating flow into (out of) side channel, with velocity vectors ( $v_{\text{sec}}, w$ ) in the cross-sectional plane.

toward the side channel. This feature is known to linearly decrease the side channel discharge (de Ruijsscher et al., 2019).

The longitudinal variation in the inflow angle is reasonably well predicted by the analytical potential flow model. At the sill ( $y = 0$ ), the outflow angle is described by

$$\begin{aligned} \phi &= \arctan\left(\frac{u}{v}\right), \\ \phi(y=0) &= \arctan\left(\frac{\alpha}{1 - \frac{\alpha}{2\pi} \ln(\hat{x}^2/(\hat{x}-1)^2)}\right) \\ &\approx \arctan(\alpha) + \frac{4\alpha^2}{(1+\alpha^2)\pi} \left(\hat{x} - \frac{1}{2}\right). \end{aligned} \quad (11)$$

A first-order Taylor expansion around  $\hat{x} = 1/2$  is used for the approximation. This approximation corresponds to the linear increase in  $\phi$  with increasing  $x$  in the main channel close to the sill (Figures 7a and 7b). Although  $\phi$  is slightly underestimated, the phenomenon is qualitatively well reproduced by this simple model. The nonlinearized version of equation (11) even captures the sudden increase in  $\phi$  as  $x \rightarrow 244$  m ( $\hat{x} \rightarrow 1$ , close to the downstream end of the sill, Figure 6a). The variation in  $\phi$  over the hydrograph is not captured (Figures 7b and 7c).

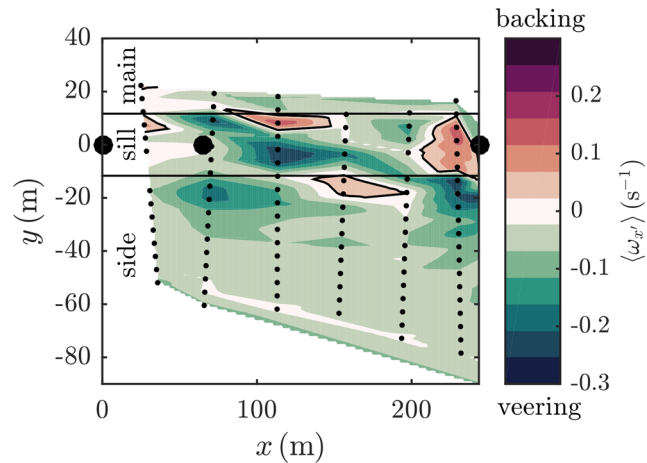


**Figure 10.** Spatial distribution of the depth-averaged vorticity component  $(\omega_{x'})$ . Areas of backing (top flow rotated toward the main channel) are surrounded by a solid contour. Horizontal solid lines indicate the edges of the sill plateau, with the side channel on the lower half of the graph. Small dots indicate velocity cells used for integration, and large dots indicate existing navigation poles.

### 3.1.3. Vertical Flow Variation

Apart from an increasing velocity away from the bed (equation (3)), the velocity magnitude  $|\vec{u}|$  in the side channel increases in the downstream direction as a result of decreasing proximity to the bifurcation point (contours in Figures 9a and 9c). To illustrate the cross-sectional velocity pattern over the sill and in the side channel, the secondary velocity pattern (i.e., in the plane of the cross section) is shown in Figures 9b and 9d for cross sections at the halfway point and downstream end of the sill, respectively. An inflow of water into the side channel is observed, as expected, although for  $x = 113$  m, close to the bed in the side channel, the flow is locally directed toward the main channel (Figure 9b). This information hints at a vertical secondary circulation cell, which is clearly not present at the shallower cross section more downstream (Figure 9d).

As observed from the flow velocity vectors in Figures 9a and 9c, veering (clockwise rotation over height) of the flow velocity vector over depth is also observed, with the flow higher in the water column being directed more into the side channel (see definition in Figure 4). Using the definition of equation (4) for  $\omega_{x'}$ , backing/veering of the flow velocity vector is illustrated in a spatial sense in Figure 10. A clear veering effect is observed at the side channel side of the sill, which decreases with increasing distance from the sill. On the plateau of the sill, the effect varies in the downstream direction from close to 0 via veering to backing, with the largest backing at the most downstream end of the sill and the largest veering in the center of the

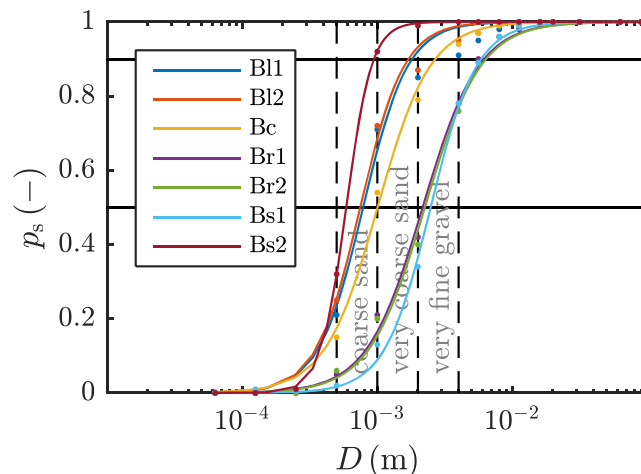


**Figure 11.** Sieving curves of the bed samples in the main channel (left Bl, center Bc, right Br) and the side channel (Bs), gathered on 24 and 27 November 2017, respectively. Sample locations are indicated in Figure 3.

**Table 3**  
Median and 90th Percentile Particle Diameter of Bed Samples

		$D_{50}$ (mm)	$D_{90}$ (mm)
main left	B11	0.785	1.81
	B12	0.747	1.70
main center	Bc	1.00	2.69
main right	Br1	2.17	6.18
	Br2	2.25	6.40
side	Bs1	2.48	5.88
	Bs2	0.589	0.945

Note. Sample locations are indicated in Figure 3.

sill. The veering in the side channel is most likely a geometrical effect caused by sheltering of the lower part of the water column by the sill, resulting in inflow only in the upper part of the water column and a more LTD-aligned flow in the lower part of the water column.

### 3.2. Sediment Transport Over a Side Weir

#### 3.2.1. Bed Load Sediment Transport

From bed samples taken in 2017, the characteristic sediment diameters  $D_{50}$  and  $D_{90}$  were derived using equations (5) and (6), as shown in Figure 11 and Table 3. There appears to be significant transverse sediment sorting, with much finer sediment on the left side of the river, which is consistent with earlier observations in the Waal River (Wilbers & ten Brinke, 2003; Wilbers, 2004). On the right side of the river, minimal differences are observed between sediment particle diameters in the main and side channels. However, significant fining occurs more downstream in the side channel.

In the main (side) channel, shear velocities  $u_*$  are higher (lower) than the critical shear velocity for initiation of motion  $u_{*,c}$  over the depth range where the logarithmic velocity profile of equation (3) applies (Figure 12). Thus, the very coarse sand of the bed can be transported as bed load in the main channel but not in the side channel. This explains the sediment fining in the downstream direction. At the sloping surface of the LTD, the velocity profile does not obey the logarithmic equation near the bed. Here, the velocity increases more rapidly with increasing distance from the bottom, causing relatively large velocities close to the bed. As  $u_* > u_{*,cr}$  and even larger shear occurs near the sloping LTD surface, sediment is likely to be transported in bed load mode over the sill.

#### 3.2.2. Suspended Load Sediment Transport

Due to the extremely low discharge at the time that water samples were taken (11 October 2018), a uniform suspended sediment concentration of  $SSC = 16 \pm 2 \text{ mg L}^{-1}$  has been measured for the water samples taken on 11 October 2018 in the main channel. Typical particle size characteristics are  $D_{50} < 16 \mu\text{m}$  and  $D_{90} = 63 \mu\text{m}$ , indicating that the suspended sediment consists of coarse silt. With calibration from ADCP

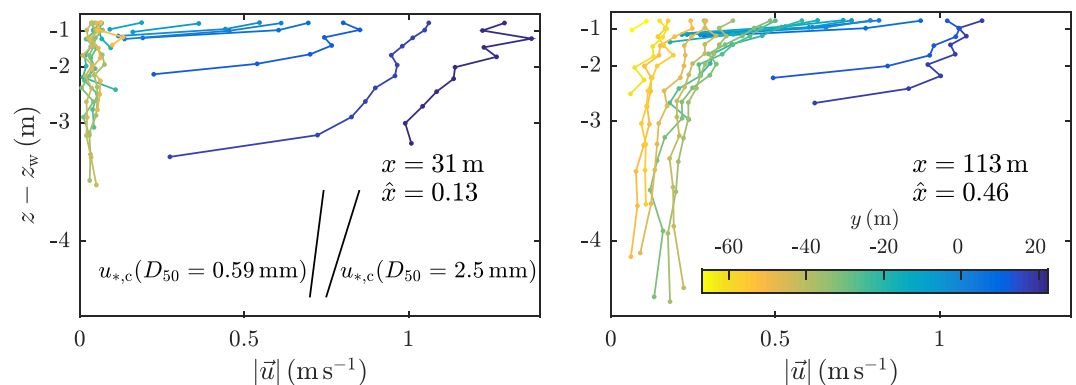


**Figure 12.** Logarithmic velocity profiles at (a)  $x = 31 \text{ m}$  and (b)  $x = 113 \text{ m}$  downstream from the upstream pole for different transverse distances. The slope of the two black lines denotes critical shear velocities  $u_{*,c}$  for typical particle sizes near the side weir.

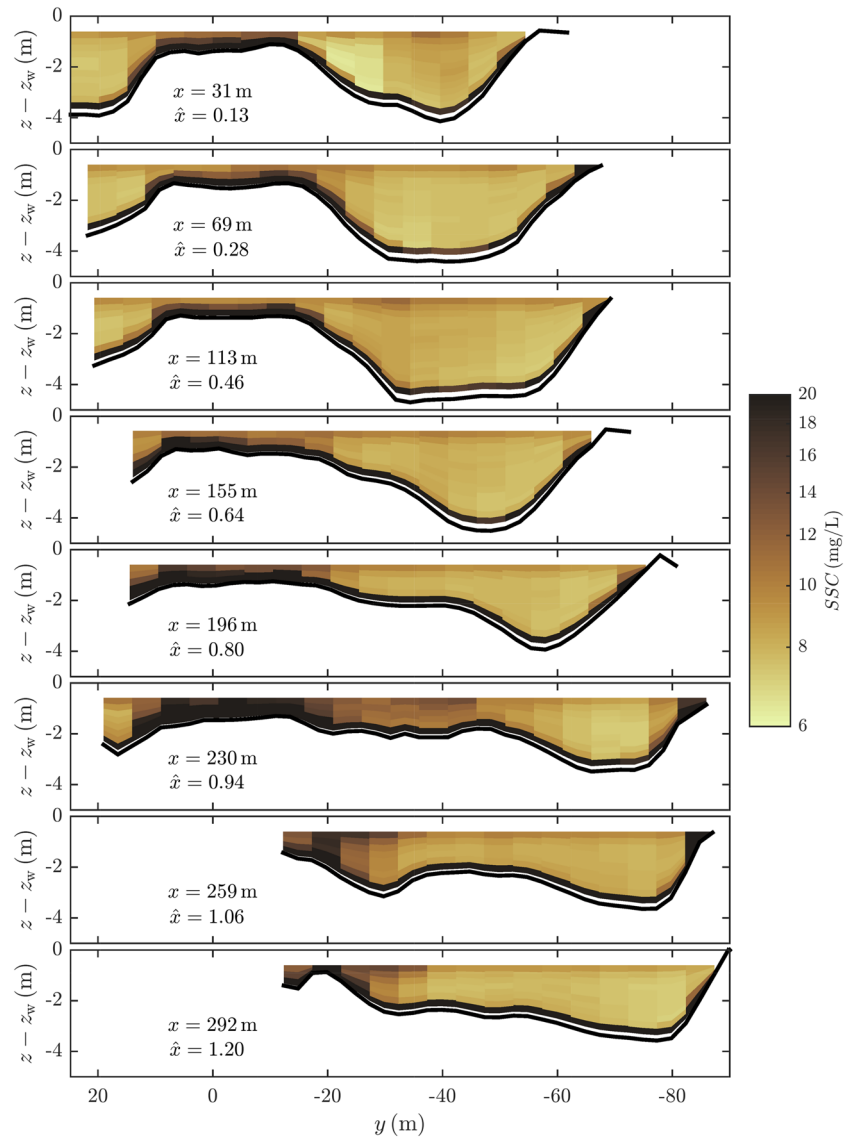


**Figure 13.** Suspended sediment over the cross sections upstream in the side channel (11 October 2018). From top to bottom in downstream direction. The side channel is located at  $y < 0$ .

backscatter, the suspended sediment concentration is calculated over the six most upstream side channel cross sections, which extend partly over the LTD sill. Apart from slight local variation, the suspended sediment concentration in the side channel is rather uniform (Figure 13). Larger variations occur locally over the sill, and larger sediment concentration values are observed there in general.

The possibility of suspended sediment transport occurring locally even for larger particles is confirmed by comparison of the shear velocity  $u_*$  with the settling velocity  $w_s$  for  $D_{50} = 2.17$  mm (main channel close to the sill). For the main channel, we applied the fit to the upper part of the water column, as the lower part is largely influenced by the sloping sill. For the side channel, we applied the fit to the lower part of the water column, as the upper part is dominated by the inflow of water over the sill. Both these choices result in a lower bound for  $u_*$  and hence for  $u_*/w_s$ . In the main channel and part of the side channel,  $u_*/w_s > 1$ , and in most of the side channel,  $u_*/w_s > 0.4$ , which is the limit for suspended sediment transport according to van Rijn (1984) (Figure 14). Therefore, suspended sediment transport likely occurs on the top of and on both sides of the sill even at the very low discharge during the measurement day. However, the larger particles found in the bed material are likely to settle.

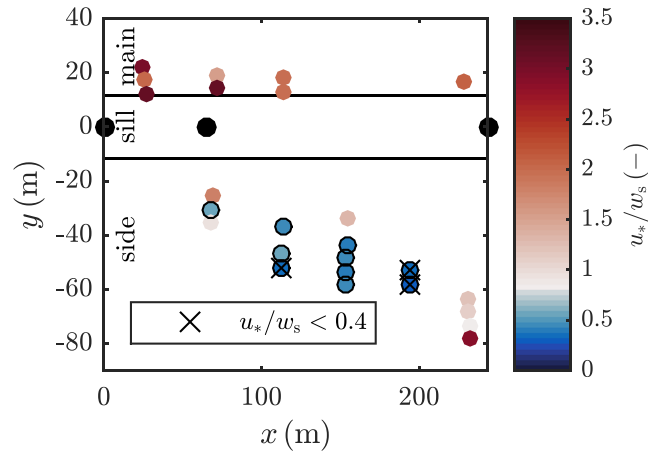


**Figure 14.** Ratio of shear velocity to settling velocity  $u_*/w_s$  in main and side channels. Blue colors with black outline indicate  $u_*/w_s < 0.8$  (the criterion of Bagnold, 1966, is not met), and crosses indicate  $u_*/w_s < 0.4$  (the criterion of Van Rijn, 1984, is not met).

## 4. Discussion

### 4.1. Velocity Direction

The present field study confirms the observation of Hager (1987) that the flow angle increases with decreasing distance to the sill (Figure 6a, II in Figure 15), although those observations were based on free flow instead of submerged side weir experiments. The observation of Hager (1987) that the flow angle over the sill increases with decreasing distance to the bifurcation point is also confirmed (I in Figure 15). However, the flow angle is smaller than that in the free flow experiments, where it increases toward  $90^\circ$  at the bifurcation point. This finding is in accordance with the unpublished numerical study of van Linge (2017), who extended the model of Hager (1987) with a flow angle submergence coefficient based on Villemonte (1947).

The main differences between the described experimental case (Hager & Volkart, 1986; Hager, 1987) and the present field study are that the former contained a thin plate as a side weir with free flow conditions, whereas the latter contains a submerged, broad-crested side weir with a 1:3 slope and a downstream side channel parallel to the main channel. The submergence results in the downstream flow conditions influencing the flow over the weir, or more specific for the present case study, the presence of the downstream channel causes a strengthening of the outflow velocity component along the  $s$  axis and thus a reduction in the flow angle. Moreover, the flow in the lower part of the water column is more geometrically steered (in this case aligned with the sill), causing a veering effect (I in Figure 15), whereas backing was observed in the free flow experiments of Hager (1987). This veering is in accordance with the observations of de Ruijsscher et al. (2019) using a scale model based on the present geometry.

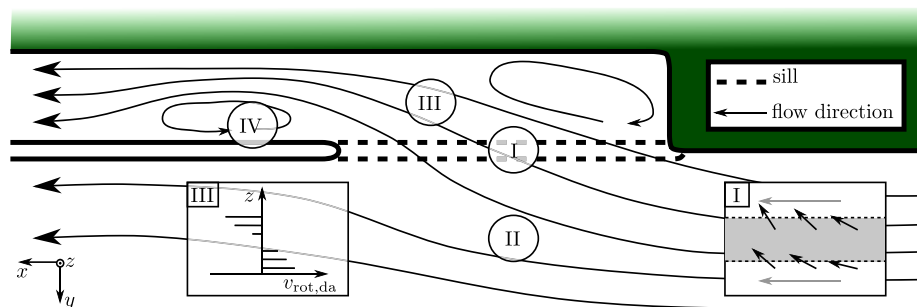


**Figure 15.** Overview of the important processes at a flow diversion toward an LTD side channel. (I)  $\partial\phi/\partial x > 0$  and  $\partial\phi/\partial z > 0$  (inset, where gray arrows indicate the flow velocity lower in the water column). (II)  $\partial\phi/\partial y < 0$  in the main channel. (III) Shear over vertical, with  $v_{rot,da}$  defined in Figure 4. (IV) Horizontal recirculation cell.

Although the logarithmic velocity profile is strictly valid only in the inner layer of the flow, several studies have shown that the validity of equation (3) extends further toward the water surface. Several examples—with  $z_b$  the bed level height—are  $3D_{84} < z - z_b < 0.2d$  (Wilcock, 1996),  $0.05 < (z - z_b)/d < 0.5$  (Smart, 1999),  $0.25 < (z - z_b)/d < 0.7$  (Bagherimiyab & Lemmin, 2013), and throughout the whole water column outside the viscous sublayer, as long as the data support a linear relationship between  $\log_{10}(z - z_b)$  and  $|\bar{u}|$  (Cardoso et al., 1989). This finding confirms that our approach of determining  $u_*$  from the slope of the logarithmic velocity profile in  $(\log_{10}z, |\bar{u}|)$  space is valid.

Qualitatively, the depth-averaged flow direction over the side weir is well captured by the potential flow model of Kästner (2019) based on superposition of uniform main channel flow and lateral outflow. The underestimation of the flow angle into the side channel is likely caused by underestimation of the parameter  $\alpha = v_0/u_0$  from field observations. The velocity component  $v_0$  is estimated from the longitudinal velocity profile closest to the sill ( $y = 11$  m) but still in the main channel. Therefore, the flow cross-sectional area parallel to the sill is larger than it is on the sill plateau, which will cause a lower transverse velocity component compared with the sill plateau:  $v_0$  and hence  $\alpha$  are underestimated. According to the linearized equation (11), this will not only increase the predicted value of  $\phi$  but also slightly increase  $\partial\phi/\partial x$ .

Another cause of the discrepancy between the results of the potential flow model and the observed flow angle values in the field is the simplification of reality and hence the negligence of various physical processes. Roughness of both the main channel bed and the rip-rap material of sill and LTD is neglected, as well as convergence and divergence of the flow at the sill. Apparently these processes do not affect the general qualitative flow pattern significantly.

#### 4.2. Secondary Flow Patterns in the Side Channel

The cross-sectional velocity profile in the side channel (Figure 9b) and, to a lesser extent, the velocity profile with respect to the depth-averaged velocity (Figures 9a and 9c) suggest a vertical secondary circulation cell in the side channel. This might be caused by (1) a difference in roughness between the sandy side channel and the rocky sill (Vermaas et al., 2011) or (2) the curved flow into the side channel, as expected at bifurcations (Bulle, 1926; Blanckaert et al., 2013; Dietrich & Smith, 1984; Dutta, 2017; Kästner & Hoitink, 2019). However, the velocity profiles over depth show very low values for  $\partial|\bar{u}|/\partial z$  in the lower part of the water column of the side channel in contrast to the upper part (Figure 12). This finding indicates that the sill causes sheltering of the lower part of the water column, which excludes the first possible cause of a secondary circulation. The second possible cause is also excluded because the water depth over the sill is very limited during the conditions described in Figure 9, which would certainly block the spiral flow over the sill. Thus, no vertical circulation cell is observed here; however, vertical shear is caused by sheltering of the lower part of the water column by the sill (III in Figure 15).

Another secondary velocity pattern observed is the downstream horizontal recirculation cell against the LTD slope (Figures 3 and 5, IV in Figure 15). This phenomenon is consistent with the lab observations of Hager (1987), who observed a downstream increasing flow angle over the side weir up to  $\phi = 90^\circ$  at the bifurcation point and hence a downstream discharge of  $Q_{\text{side,d}} = 0 \text{ m}^3 \text{ s}^{-1}$ . This is also analytically obtained from the potential flow model in equation (11) and Figure 7b, where  $\phi$  rapidly increases close to the LTD head. The recirculation cell was also observed in experiments with a 1:60 physical scale model of the present field site by de Ruijsscher et al. (2019), revealing a persistent flow separation phenomenon.

#### 4.3. Sediment Transport

Comparison of the slope of the logarithmic velocity profiles in  $(\log_{10}z, |\bar{u}|)$  space with typical values of the critical shear velocity (Figure 12) is performed without taking into account the effects of a transverse bed slope and the flow alignment thereon. When a correction for these effects is applied, it appears that the underestimation of  $u_{*c}$  is only 5% for an inflow angle of  $\phi = 30^\circ$  (Appendix A1). Given the fact that near the sloping bed of the LTD the velocity profile seems to not obey the logarithmic profile, this underestimation is negligible.

From the limited data on both bed load and suspended sediment, it is difficult to draw solid conclusions on whether sediment is transported in bed load mode over the LTD sill. However, given the spatial distribution of bed particle sediment size (Table 3 and Figure 11) and the large shear stress over the sill (Figure 12), this is very likely the case. Because sediment does not accumulate in the side channel at a substantial rate, either there is side channel bed load transport at high discharges (no field confirmation) or the amount of bed load

sediment transported over the sill is limited. Moreover, assuming that the morphological stability of an LTD side channel is well described by general side channel stability theory (van Denderen et al., 2018), we should conclude that the two-channel system is stable, despite almost all discharge being conveyed by the main channel. As a substantial part of the discharge is still conveyed by the side channel in the field, the presence of the sill appears to have a significant contribution in the morphological evolution of a side channel.

The sediment nonuniformity might affect the applicability of the Bagnold (1966) and van Rijn (1984) criteria, as these are based on a uniform sediment assumption, taken as  $D_{50}$ . We do not expect this assumption to significantly affect our conclusions, as both criteria are only used as a rough indicator for the possibility of suspended load sediment transport in Figure 14. Yet as  $u_{*c}$  decreases with decreasing sediment particle size, this even enhances the possibility of at least the finer sediment fraction being transported in suspension in the side channel. In order to gain more insight in sediment transport toward a side channel separated from a river by an LTD, both bed load and suspended load, a thorough numerical study using a particle tracking model would be beneficial.

For sharp-crested plain weirs, it was earlier observed that scour occurs downstream of the weir due to a combination of thickening of the jet flow downstream of the weir and turbulent mixing of the jet flow with the tailwater (Guan et al., 2015, 2016). Such scour is not observed in the present study, which is likely caused by a combination of the flow behind the weir being geometrically steered and the presence of a side slope at the weir, preventing tailwater formation as occurs at sharp-crested plain weirs. Moreover, spare rip-rap is stored in the side channel, directly next to the sill, possibly preventing erosion.

## 5. Conclusions

A field campaign was conducted to understand the processes controlling the diversion of flow and sediment toward a side channel separated from the river by a LTD. A sill or submerged weir was located at the bifurcation of the main river and the side channel. In the main channel next to the sill, the angle between the local flow velocity vector and the principal direction of the main channel increases with decreasing lateral and longitudinal distance to the bifurcation point. This bifurcation point corresponds to the LTD head. The inflow angle over the sill negatively correlates with the upstream water level, with variations on the order of  $10^\circ$ . Vertical shear is observed in the side channel caused by sheltering of the lower part of the water column by the sill. The variation in the flow direction over depth is governed by the flow being more geometrically steered (aligned with the sill) lower in the water column, causing a veering effect.

The general depth-averaged main channel flow pattern and the longitudinal variation in the flow angle along the sill are qualitatively well reproduced with a uniform-depth, potential flow model consisting of a superposition of uniform main channel flow and lateral outflow. However, the model slightly underestimates the measured flow angles, which is likely due to underestimated model input parameters from field conditions and the lack of representation of roughness and flow conversion effects in the model.

Sediment is likely transported in bed load mode over the sill, although in limited amounts. Due to the lower velocities and shear velocities in the side channel, sediment fining occurs in the downstream direction. Suspended sediment concentrations are especially high over the sill, and the ratio of the shear velocity to settling velocity ( $u_* / w_s$ ) is larger than the critical value for the onset of suspension, demonstrating that suspended sediment transport over the sill occurs even under low discharge conditions.

We conclude that our hypotheses on flow, sediment import and morphological stability—as formulated at the end of section 1—are largely confirmed. The flow behaves qualitatively as free flow over a side weir, although a submergence correction factor needs to be taken into account for quantitative predictions. The depth-averaged main channel flow near the sill is qualitatively well reproduced with a uniform depth, potential flow model consisting of a superposition of uniform main channel flow and lateral outflow. The morphological stability of the side channel is largely influenced by the presence of the sill via general bifurcation stability mechanisms: The sloping surface limits but does not prevent bed load transport into the side channel, and the inlet step at the bifurcation increases the fraction of the total sediment volume entering the side channel in suspended mode.

## Appendix A: Critical Shear Stress and Corrections Thereon

The critical Shields parameter, or critical nondimensional shear stress, is a nondimensionalization of the shear stress at the critical value for initiation of motion. Here we will use the parametrized expression by

Soulsby and Whitehouse (1997) from the original experimentally determined Shields curve (Shields, 1936), as given by

$$\theta_c = \frac{0.3}{1 + 1.2D_*} + 0.055 (1 - \exp[-0.02D_*]) . \quad (A1)$$

In this equation  $D_*$  is the nondimensional particle diameter given by

$$D_* = D_{50} \left( \frac{(\rho_s - \rho_w) g}{\rho_w \nu^2} \right)^{1/3} , \quad (A2)$$

where  $\rho_w$  and  $\rho_s$  are the density of water and sediment, respectively,  $g$  is the gravitational acceleration, and  $\nu$  is the kinematic viscosity. The dimensional critical shear stress  $\tau_c$  or dimensionless critical Shields parameter can also be expressed in units of velocity, as the critical shear velocity  $u_{*,c}$ , given by

$$u_{*,c} = \sqrt{\frac{\tau_c}{\rho_w}} = \sqrt{\frac{\theta_c (\rho_s - \rho_w) g D_{50}}{\rho_w}} . \quad (A3)$$

In accordance with the unpublished report of Jammers (2017), a correction factor that takes into account both the effect of a transverse bed slope and a slope that is not aligned with the flow is determined. Three angles are of importance: the transverse bed slope angle  $\alpha$ , the flow angle  $\phi$  (positive for flow into the side channel), and the angle of repose  $\varphi_r$ . In the present study, we use fixed values of  $\alpha = \arctan(1/3)$  and  $\varphi_r = 30^\circ$ . A correction factor  $\tilde{\theta}_c^{(\alpha,\phi)}$  for the critical Shields parameter is defined as

$$\theta_{c,\phi} = \tilde{\theta}_c^{(\alpha,\phi)} \theta_{c,0} , \quad (A4)$$

with

$$\tilde{\theta}_c^{(\alpha,\phi)} = \frac{\tan(\alpha) \tan(\phi)}{\sqrt{1 + \frac{\tan^2(\phi)}{\cos^2(\alpha)}} \tan(\varphi_r)} + \cos(\alpha) \sqrt{1 - \frac{\tan^2(\alpha)}{\left(1 + \frac{\tan^2(\phi)}{\cos^2(\alpha)}\right) \tan^2(\varphi_r)}} . \quad (A5)$$

## Acknowledgments

This research is part of the research program RiverCare, supported by the Netherlands Organization for Scientific Research (NWO), and which is partly funded by the Ministry of Economic Affairs and Climate Policy under Grant P12-14 (Perspective Programme). Additional funding is provided by Rijkswaterstaat Oost-Nederland within the WaalSamen program. The data and scripts used in this study are publicly available online (<https://doi.org/10.4121/uuid:a2b6bb99-b984-4d30-bbb8-bacd80f251ad>). The Matlab toolbox for processing ADCP data, developed by Bart Vermeulen, is freely available online (<https://sourceforge.net/projects/adcpools>).

## References

- Bagherimiyab, F., & Lemmin, U. (2013). Shear velocity estimates in rough-bed open-channel flow. *Earth Surface Processes and Landforms*, 38(14), 1714–1724. <https://doi.org/10.1002/esp.3421>
- Bagnold, R. A. (1966). An approach to the sediment transport problem from general physics. Geology Survey Professional Paper 422-I.
- Barkdoll, B. D. (1997). Sediment control at lateral diversions (Ph.D. Thesis).
- Blanckaert, K., Kleinhans, M. G., McLelland, S. J., Uijttewaal, W. S. J., Murphy, B. J., van de Kruijs, A., et al. (2013). Flow separation at the inner (convex) and outer (concave) banks of constant-width and widening open-channel bends. *Earth Surface Processes and Landforms*, 38(7), 696–716. <https://doi.org/10.1002/esp.3324>
- Bolla Pittaluga, M., Coco, G., & Kleinhans, M. G. (2015). A unified framework for stability of channel bifurcations in gravel and sand fluvial systems. *Geophysical Research Letters*, 42, 7521–7536. <https://doi.org/10.1002/2015GL065175>
- Bolla Pittaluga, M., Repetto, R., & Tubino, M. (2003). Channel bifurcation in braided rivers: Equilibrium configurations and stability. *Water Resources Research*, 39(3), 1046. <https://doi.org/10.1029/2001WR001112>
- Borghei, S. M., Vatannia, Z., Ghodsian, M., & Jalili, M. R. (2003). Oblique rectangular sharp-crested weir. *Proceedings of the Institution of Civil Engineers Water Maritime Engineering*, 156(2), 185–191. <https://doi.org/10.1680/wame.2003.156.2.185>
- Bos, M. G. (1976). Discharge measurement structures (20): International Institute for Land Reclamation and Improvement, Wageningen, The Netherlands.
- Bremen, R., & Hager, W. H. (1989). Experiments in side-channel spillways. *Journal of Hydraulic Engineering*, 115(5), 617–635.
- Bulle, H. (1926). *Untersuchungen über die Geschiebeableitung bei der Spaltung von Wasserläufen, Forschungsarbeiten auf dem Gebiete des Ingenieurwesens* (Vol. 283). Verein Deutscher Ingenieure. in German.
- Cardoso, A. H., Graf, W. H., & Gust, G. (1989). Uniform flow in a smooth open channel. *Journal of Hydraulic Research*, 27(5), 603–616. <https://doi.org/10.1080/00221688909499113>
- Cheng, N.-S. (2009). Comparison of formulas for drag coefficient and settling velocity of spherical particles. *Powder Technology*, 189(3), 395–398. <https://doi.org/10.1016/j.powtec.2008.07.006>
- Collas, F. P. L., Buijse, A. D., van den Heuvel, L., van Kessel, N., Schoor, M. M., Eerden, H., & Leuven, R. S. E. W. (2018). Longitudinal training dams mitigate effects of shipping on environmental conditions and fish density in the littoral zones of the river Rhine. *Science of the Total Environment*, 619–620, 1183–1193. <https://doi.org/10.1016/j.scitotenv.2017.10.299>
- de Ruijscher, T. V., Hoitink, A. J. F., Naqshband, S., & Paarlberg, A. J. (2019). Bed morphodynamics at the intake of a side channel controlled by sill geometry. *Advances in Water Resources*, 134, 103452. <https://doi.org/10.1016/j.advwatres.2019.103452>
- Deines, K. L. (1999). Backscatter estimation using broadband acoustic Doppler current profilers. In S. P. Anderson, E. A. Terray, J. A. Rizoli White, & A. J. Williams III, (Eds.) *Proceedings of the IEEE Sixth Working Conference on Current Measurement* (pp. 249–253).
- Dietrich, W. E., & Smith, J. Dungan (1984). Bed load transport in a river meander. *Water Resources Research*, 20(10), 1355–1380. <https://doi.org/10.1029/WR020i10p01355>

- Dutta, S. (2017). Bulle-effect and its implications for morphodynamics of river diversions (Ph.D. Thesis). <http://hdl.handle.net/2142/97290>
- Edmonds, D. A., & Slingerland, R. L. (2008). Stability of delta distributary networks and their bifurcations. *Water Resources Research*, *44*, W09426. <https://doi.org/10.1029/2008WR006992>
- Eerden, H., van Riel, E., de Koning, R., Zemlak, E., & Aziz, N. (2011). Integraal ontwerp pilot langsdammen Waal: Rijkswaterstaat Oost-Nederland, Arnhem, The Netherlands. in Dutch.
- El-Khashab, A., & Smith, Kenneth V. H. (1976). Experimental investigation of flow over side weirs. *Journal of Hydraulic Engineering Division ASCE*, *102*(HY9), 1255–1268.
- Eleftheriou, A., & Moore, D. C. (2013). Macrofauna techniques, (fourth). In A. Eleftheriou (Ed.), *Methods for the study of marine benthos* (pp. 175–252). Oxford: John Wiley & Sons, Ltd.
- Guan, D., Melville, B. W., & Friedrich, H. (2015). Live-bed scour at submerged weirs. *Journal of Hydraulic Engineering*, *141*(2), 04014071. [https://doi.org/10.1061/\(ASCE\)HY.1943-7900.0000954](https://doi.org/10.1061/(ASCE)HY.1943-7900.0000954)
- Guan, D., Melville, B. W., & Friedrich, H. (2016). Local scour at submerged weirs in sand-bed channels. *Journal of Hydraulic Research*, *54*(2), 172–184. <https://doi.org/10.1080/00221686.2015.1132275>
- Hager, W. H. (1987). Lateral outflow over side weirs. *Journal of Hydraulic Engineering*, *113*(4), 491–504. [https://doi.org/10.1061/\(ASCE\)0733-9429\(1987\)113:4\(491\)](https://doi.org/10.1061/(ASCE)0733-9429(1987)113:4(491))
- Hager, W. H., & Volkart, P. U. (1986). Distribution channels. *Journal of Hydraulic Engineering*, *112*(10), 935–952. [https://doi.org/10.1061/\(ASCE\)0733-9429\(1986\)112:10\(935\)](https://doi.org/10.1061/(ASCE)0733-9429(1986)112:10(935))
- Hardy, R. J., Lane, S. N., & Yu, D. (2011). Flow structures at an idealized bifurcation: A numerical experiment. *Earth Surface Processes and Landforms*, *36*(15), 2083–2096. <https://doi.org/10.1002/esp.2235>
- Havinga, H. (2016). Visie op het rivierbeheer van de Rijn: Rijkswaterstaat Oost-Nederland, Arnhem, The Netherlands. in Dutch.
- Hill, D. C., Jones, S. E., & Prandle, D. (2003). Derivation of sediment resuspension rates from acoustic backscatter time-series in tidal waters. *Continental Shelf Research*, *23*(1), 19–40. [https://doi.org/10.1016/S0278-4343\(02\)00170-X](https://doi.org/10.1016/S0278-4343(02)00170-X)
- Hoitink, A. J. F., & Hoekstra, P. (2005). Observations of suspended sediment from ADCP and OBS measurements in a mud-dominated environment. *Coastal Engineering*, *52*(2), 103–118. <https://doi.org/10.1016/j.coastaleng.2004.09.005>
- Holdaway, G. P., Thorne, P. D., Flatt, D., Jones, S. E., & Prandle, D. (1999). Comparison between ADCP and transmissometer measurements of suspended sediment concentration. *Continental Shelf Research*, *19*(3), 421–441. [https://doi.org/10.1016/S0278-4343\(98\)00097-1](https://doi.org/10.1016/S0278-4343(98)00097-1)
- Huthoff, F., Paarlberg, A. J., Barneveld, H., & van der Wal, M. (2011). Rivierkundig onderzoek WaalSamen: Pilotstudie langsdammen (PR2096.10): HKV Consultants, Lelystad, The Netherlands. in Dutch.
- Jammers, S. M. M. (2017). Sediment transport over sills of longitudinal training dams. <http://resolver.tudelft.nl/uuid:4570fe94-c2f2-4d4c-96a0-fb53d7e7dc3f>
- Kästner, K., & Hoitink, A. J. F. (2019). Flow and suspended sediment division at two highly asymmetric bifurcations in a river delta: Implications for channel stability. *Journal of Geophysical Research: Earth Surface*, *124*, 2358–2380. <https://doi.org/10.1029/2018JF004994>
- Kästner, K. (2019). Multi-scale monitoring and modelling of the Kapuas River Delta (Ph.D. Thesis).
- Kleinhans, M. G., Ferguson, R. I., Lane, S. N., & Hardy, R. J. (2013). Splitting rivers at their seams: Bifurcations and avulsion. *Earth Surface Processes and Landforms*, *38*(1), 47–61. <https://doi.org/10.1002/esp.3268>
- Le, T. B., Crosato, A., Mosselman, E., & Uijtewaal, W. S. J. (2018). On the stability of river bifurcations created by longitudinal training walls. Numerical investigation. *Advances in Water Resources*, *113*, 112–125. <https://doi.org/10.1016/j.advwatres.2018.01.012>
- Le, T. B., Crosato, A., & Uijtewaal, W. S. J. (2018). Long-term morphological developments of river channels separated by a longitudinal training wall. *Advances in Water Resources*, *113*, 73–85. <https://doi.org/10.1016/j.advwatres.2018.01.007>
- Lee, K. L., & Holley, E. R. (2002). Physical modeling for side-channel weirs (02-2): Center for Research in Water Resources, University of Texas at Austin. [https://repositories.lib.utexas.edu/bitstream/handle/2152/6891/crwr\\_onlinereport02-2.pdf](https://repositories.lib.utexas.edu/bitstream/handle/2152/6891/crwr_onlinereport02-2.pdf)
- Michelazzo, G., Minatti, L., Paris, E., & Solari, L. (2016). Side weir flow on a movable bed. *Journal of Hydraulic Engineering*, *142*(6), 04016007. [https://doi.org/10.1061/\(ASCE\)HY.1943-7900.0001128](https://doi.org/10.1061/(ASCE)HY.1943-7900.0001128)
- Mosselman, E., Huisink, M., Koomen, E., & Seijmonsbergen, A. C. (1995). Morphological changes in a large braided sand-bed river. In E. J. Hickin (Ed.), *River geomorphology* (pp. 235–247). Oxford: John Wiley & Sons, Inc.
- Neary, V. S., & Odgaard, A. J. (1993). Three-dimensional flow structure at open-channel diversions. *Journal of Hydraulic Engineering*, *119*(11), 1223–1230. [https://doi.org/10.1061/\(ASCE\)0733-9429\(1993\)119:11\(1223\)](https://doi.org/10.1061/(ASCE)0733-9429(1993)119:11(1223))
- Neary, V. S., Sotiropoulos, F., & Odgaard, A. J. (1999). Three-dimensional numerical model of lateral-intake inflows. *Journal of Hydraulic Engineering*, *125*(2), 126–140. [https://doi.org/10.1061/\(ASCE\)0733-9429\(1999\)125:2\(126\)](https://doi.org/10.1061/(ASCE)0733-9429(1999)125:2(126))
- Oele, E. (1978). Sand and gravel from shallow seas. *Geologie en Mijnbouw*, *57*(1), 45–54.
- Paris, E., Solari, L., & Bechi, G. (2012). Applicability of the De Marchi hypothesis for side weir flow in the case of movable beds. *Journal of Hydraulic Engineering*, *138*(7), 653–656. [https://doi.org/10.1061/\(ASCE\)HY.1943-7900.0000566](https://doi.org/10.1061/(ASCE)HY.1943-7900.0000566)
- Ramamurthy, A. S., & Satish, M. G. (1988). Division of flow in short open channel branches. *Journal of Hydraulic Engineering*, *114*(4), 428–438. [https://doi.org/10.1061/\(ASCE\)0733-9429\(1988\)114:4\(428\)](https://doi.org/10.1061/(ASCE)0733-9429(1988)114:4(428))
- Sassi, M. G., Hoitink, A. J. F., & Vermeulen, B. (2012). Impact of sound attenuation by suspended sediment on ADCP backscatter calibrations. *Water Resources Research*, *48*, W09520. <https://doi.org/10.1029/2012WR012008>
- Shields, A. (1936). Anwendung der Ähnlichkeitsmechanik und der Turbulenzforschung auf die Geschiebepbewegung. *Preussische Versuchsanstalt für Wasserbau und Schiffbau*, *26*, 1–26. in German.
- Slingerland, R., & Smith, N. D. (1998). Necessary conditions for a meandering-river avulsion. *Geology*, *26*(5), 435–438. [https://doi.org/10.1130/0091-7613\(1998\)026h0435:NCFAMRi2.3.CO;2](https://doi.org/10.1130/0091-7613(1998)026h0435:NCFAMRi2.3.CO;2)
- Smart, G. M. (1999). Turbulent velocity profiles and boundary shear in gravel bed rivers. *Journal of Hydraulic Engineering*, *125*(2), 106–116. [https://doi.org/10.1061/\(ASCE\)0733-9429\(1999\)125:2\(106\)](https://doi.org/10.1061/(ASCE)0733-9429(1999)125:2(106))
- Soulsby, R. L., & Whitehouse, R. J. S. (1997). Threshold of sediment motion in coastal environments. In *Pacific coasts and ports '97: Proceedings of the 13th australasian coastal and ocean engineering conference and the 6th australasian port and harbour conference; volume 1*, Centre for Advanced Engineering, University of Canterbury, pp. 145–150.
- van Denderen, R. P., Schielen, R. M. J., Blom, A., Hulscher, S. J. M. H., & Kleinhans, M. G. (2018). Morphodynamic assessment of side channel systems using a simple one-dimensional bifurcation model and a comparison with aerial images. *Earth Surface Processes and Landforms*, *43*(6), 1169–1182. <https://doi.org/10.1002/esp.4267>
- van Linge, B. W. (2017). Hydraulic evaluation of longitudinal training dams. <http://resolver.tudelft.nl/uuid:63160c45-f3ed-4ad2-84c8-9a1db1e04f0a>
- van Rijn, L. C. (1984). Sediment transport, Part II: Suspended load transport. *Journal of Hydraulic Engineering*, *110*(11), 1613–1641. [https://doi.org/10.1061/\(ASCE\)0733-9429\(1984\)110:11\(1613\)](https://doi.org/10.1061/(ASCE)0733-9429(1984)110:11(1613))

- Vermaas, D. A., Uijttewaal, W. S. J., & Hoitink, A. J. F. (2011). Lateral transfer of streamwise momentum caused by a roughness transition across a shallow channel. *Water Resources Research*, *47*, W02530. <https://doi.org/10.1029/2010WR010138>
- Vermeulen, B., Sassi, M. G., & Hoitink, A. J. F. (2014). Improved flow velocity estimates from moving-boat ADCP measurements. *Water Resources Research*, *50*, 4186–4196. <https://doi.org/10.1002/2013WR015152>
- Villemonte, J. R. (1947). Submerged-weir discharge studies. *Engineering News-Record*, *139*, 866–869.
- von Kármán, Th. (1930). Mechanische Ähnlichkeit und Turbulenz. *Nachrichten von der Gesellschaft der Wissenschaften zu Göttingen, Mathematisch-Physikalische Klasse*, 58–76. in German.
- Wilbers, A. W. E. (2004). The development and hydraulic roughness of subaqueous dunes (Ph.D. Thesis).
- Wilbers, A. W. E., & ten Brinke, W. B. M. (2003). The response of subaqueous dunes to floods in sand and gravel bed reaches of the Dutch Rhine. *Sedimentology*, *50*(6), 1013–1034. <https://doi.org/10.1046/j.1365-3091.2003.00585.x>
- Wilcock, P. R. (1996). Estimating local bed shear stress from velocity observations. *Water Resources Research*, *32*(11), 3361–3366. <https://doi.org/10.1029/96WR02277>